REPORT

Time-resolved ultrastructure of the cortical actin cytoskeleton in dynamic membrane blebs

Aleksandra S. Chikina[1,2] , Tatyana M. Svitkina[2] , and Antonina Y. Alexandrova[1]

Membrane blebbing accompanies various cellular processes, including cytokinesis, apoptosis, and cell migration, especially invasive migration of cancer cells. Blebs are extruded by intracellular pressure and are initially cytoskeleton-free, but they subsequently assemble the cytoskeleton, which can drive bleb retraction. Despite increasing appreciation of physiological significance of blebbing, the molecular and, especially, structural mechanisms controlling bleb dynamics are incompletely understood. We induced membrane blebbing in human HT1080 fibrosarcoma cells by inhibiting the Arp2/3 complex. Using correlative platinum replica electron microscopy, we characterize cytoskeletal architecture of the actin cortex in cells during initiation of blebbing and in blebs at different stages of their expansion–retraction cycle. The transition to blebbing in these conditions occurred through an intermediate filopodial stage, whereas bleb initiation was biased toward filopodial bases, where the cytoskeleton exhibited local weaknesses. Different stages of the bleb life cycle (expansion, pausing, and retraction) are characterized by specific features of cytoskeleton organization that provide implications about mechanisms of cytoskeleton assembly and bleb retraction.

Introduction

The cell cortex, defined as a plasma membrane–associated (cortical) cytoskeleton, plays key roles in mechanical and dynamic properties of the cell surface (Salbreux et al., 2012; Chugh and Paluch, 2018). The significance of the cortex is particularly obvious during plasma membrane blebbing, a special type of membrane protrusion that does not require actin polymerization for extension (Charras et al., 2005; Lämmermann and Sixt, 2009; Davidson et al., 2018). The generation and subsequent retraction of blebs are both driven by myosin II–dependent cell contractility and depend on cortex properties (Charras et al., 2006; Paluch and Raz, 2013; Bergert et al., 2015). Membrane blebbing accompanies various cellular processes, including cell spreading and migration, cytokinesis, and apoptosis. Bleb-based migration is a version of amoeboid motility, which is characteristic of, for example, free-living amoeba, certain cells in developing fish or amphibian embryos, and, importantly, invasive cancer cells (Charras and Paluch, 2008; Paluch and Raz, 2013; Petrie and Yamada, 2015). Enhanced motility of cancer cells during invasion and metastasis is often associated with migration plasticity (Friedl and Wolf, 2003), one aspect of which is a switch from the mechanism of leading-edge protrusion driven by Arp2/3 complex–dependent actin polymerization (Svitkina, 2018) to that involving the formation of plasma membrane blebs extruded by intracellular pressure (Paluch and Raz, 2013).

Blebs are spherical membrane protrusions that often undergo fast expansion–retraction cycles (Charras et al., 2006; Laser-Azogui et al., 2014; Aoki et al., 2016; Sroka et al., 2016), although persistent nonretracting blebs can form in rapidly migrating cells under confinement (Liu et al., 2015; Ruprecht et al., 2015). Blebs are thought to form at the regions of the cell surface, where the plasma membrane detaches from the underlying cytoskeleton and/or the cytoskeleton exhibits local weaknesses (Paluch and Raz, 2013). During expansion, blebs are devoid of detectable cytoskeleton. Over time, the actin cytoskeleton is assembled within the bleb and drives bleb retraction in a myosin II–dependent manner (Charras et al., 2006; Jiao et al., 2018). Despite ongoing efforts (Charras et al., 2006; Bovellan et al., 2014; Eghiaian et al., 2015; Fujiwara et al., 2016; Chugh et al., 2017), the cortex structure in cells and membrane blebs remains poorly characterized at a single-filament level. To address this need, we use platinum replica electron microscopy (PREM), which is best suited for revealing detailed cytoskeleton organization (Svitkina, 2016, 2017). In PREM, the cell is rotary-shadowed with a thin layer of platinum after detergent-mediated exposure of the cytoskeleton, fixation, and critical point drying. Then, a transmission electron microscope is used to visualize fine 3D topography of the sample surface.

[1]Laboratory of Mechanisms of Carcinogenesis, N.N. Blokhin Russian Cancer Research Center, Moscow, Russia;   [2]Department of Biology, University of Pennsylvania, Philadelphia, PA.

Correspondence to Antonina Y. Alexandrova: tonya_alex@yahoo.com;   Tatyana M. Svitkina: svitkina@sas.upenn.edu;   A.S. Chikina's present address is Cell Migration and Invasion and Spatio-temporal Regulation of Antigen Presentation teams, UMR144/U932 Institut Curie, Paris, France.

Results and discussion

Membrane blebbing can be experimentally induced in multiple cell types, for example, by creating conditions limiting mesenchymal motility (Petrie and Yamada, 2015). Thus, cells migrating in 3D gels switch to blebbing after inhibition of matrix proteolysis (Wolf et al., 2003). In 2D environments, blebbing can be induced by increasing cell contractility (Sahai and Marshall, 2003; Bergert et al., 2012), limiting actin-based protrusion through inhibition of the Arp2/3 complex (Derivery et al., 2008; Bergert et al., 2012; Beckham et al., 2014), or disrupting integrin-based adhesion and simultaneously applying spatial confinement to cells (Liu et al., 2015). Many of these approaches, such as 3D confinement or poor cell–substrate adhesion, are not compatible with PREM. Therefore, we induced membrane blebbing by inhibiting the Arp2/3 complex using a specific inhibitor, CK-666 (Nolen et al., 2009).

Transition from lamellipodia to blebbing occurs through the intermediate formation of filopodia

We first characterized the CK-666–dependent induction of blebs in HT1080 fibrosarcoma cells by light microscopy (Fig. 1). By phalloidin staining, actin-rich lamellipodia and ruffles were the predominant protrusion types in control HT1080 cells (Fig. 1 A, left). After treatment with 100 µM CK-666, lamellipodia and ruffles were mostly replaced by filopodia (Fig. 1 A, middle). Such transition typically accompanies Arp2/3 complex down-regulation (Gomez et al., 2007; Suraneni et al., 2012; Wu et al., 2012). It largely occurs due to redirection of actin monomers from Arp2/3-dependent actin nucleation to formin- or Ena/VASP-dependent actin filament elongation (Yang and Svitkina, 2011; Burke et al., 2014). We observed very few blebbing cells at this CK-666 dose. However, a large fraction of cells switched to blebbing after treatment with 200 µM CK-666 (Fig. 1 A, right), while other cells still expressed the filopodial phenotype. These results suggested that the formation of filopodia may represent a transitional state between the lamellipodial and blebbing modes of protrusion when blebbing is induced by Arp2/3 complex inhibition.

For direct evaluation of the lamellipodia-to-bleb transition in individual cells, we imaged cells in the course of CK-666 treatment (Fig. 1 B and Video 1). To efficiently capture transitional states, we stepwise increased the CK-666 concentration during imaging, first from normal medium to 87.5 µM, then to 120 µM, and finally to 137 µM. Untreated cells actively formed lamellipodia and ruffles, while filopodia were infrequent (Fig. 1 B, t = –1:45). Shortly after the addition of 87.5 µM CK-666, lamellipodia largely converted into ruffles (Fig. 1 B, t = 15:10). Within a few minutes after increasing the CK-666 concentration to 120 µM, cells began to form abundant filopodia at the expense of lamellipodia and ruffles (Fig. 1 B, t = 32:05). Longer incubation with this CK-666 concentration resulted in swelling of the cell lamella at the level of filopodial bases (Fig. 1 B, t = 35:55), which was quickly followed by the initiation of blebbing (Fig. 1 B, t = 41:30). A further increase in the CK-666 concentration to 137 µM led to more vigorous blebbing and more numerous blebs (Fig. 1 B, t = 53:50). During initiation of blebbing activity, 86.7% of first blebs emerged either at the base of a filopodium or between filopodia (n = 339 blebs in 17 cells from five experiments; Fig. 1 C). To

further evaluate the degree of correlation between the bleb initiation sites and filopodia, we divided the cell perimeter into eight segments (Fig. 1 E) and determined the number of nascent blebs and filopodia in each segment (Fig. 1 F). We found a strong positive correlation (Fig. 1 G) between these numbers, as indicated by the Pearson correlation coefficient (r = 0.77 ± 0.12 [mean ± SD]; n = 9 cells), which was significantly different (P < 0.0001) from the null hypothesis (r = 0). At later times, when cells switched to constitutive blebbing, new blebs could be formed between other blebs or emerge from the tip of an existing bleb. When CK-666 was washed out, the cells stopped blebbing and resumed lamellipodial protrusion by first passing through a transient stage of filopodia formation (Fig. S1 A). An alternative Arp2/3 complex inhibitor, CK-869, also induced membrane blebbing in cells. As in the case of CK-666, this transition also included an intermediate filopodial stage (Fig. S1 B). In contrast, lamellipodial activity was not affected in the presence of an inactive CK-689 compound (Fig. S1 C).

We used kymograph analysis to examine bleb kinetics in HT1080 cells treated with 200 µM CK-666 (Fig. 1 D). The whole expansion–retraction cycle of blebs consisted of a fast expansion phase, which occurred at a rate of 0.56 ± 0.28 µm/s (mean ± SD) and lasted 9 ± 4 s (n = 123), and a slower retraction phase, which occurred on average at 0.09 ± 0.03 µm/s and lasted 71 ± 21 s (n = 120). For ∼60% of blebs, the retraction phase also included an initial phase of slow dynamics that lasted 17 ± 9 s (n = 72). During this period, blebs did not expand and either remained nearly static or retracted very slowly (Fig. 1 D, bottom). Late in the retraction phase, blebs usually lost their smooth outline and became wrinkled (Fig. 1 C), as noted previously (Charras et al., 2006; Laser-Azogui et al., 2014).

The properties and kinetic parameters of plasma membrane blebbing in our experiments were similar to those reported for other systems (Cunningham, 1995; Tournaviti et al., 2007; Charras et al., 2008). Previous studies also noted various relationships between blebs and filopodia (Yoshida and Soldati, 2006; Ma and Baumgartner, 2013; Tyson et al., 2014; Meyen et al., 2015; Goudarzi et al., 2017) or lamellipodia (Derivery et al., 2008; Bergert et al., 2012). Using acute induction of the lamellipodia-to-bleb transition, we were able to define a relationship between filopodia and blebs in more detail. We found that the transition from actin-driven protrusions to blebbing after inhibition of the Arp2/3 complex occurred through the intermediate formation of filopodia, and individual blebs were formed preferentially at the base of a filopodium or between filopodia.

Blebs are initiated at sites of sparser cytoskeleton at filopodial bases

In general, blebs are thought to form at the regions of the cell surface where the plasma membrane detaches from the underlying cytoskeleton and/or the cortical cytoskeleton exhibits local weaknesses (Paluch and Raz, 2013). These ideas have been supported by experimental induction of blebs by micropipette aspiration to detach membrane from the cortical cytoskeleton (Rentsch and Keller, 2000; Maugis et al., 2010) or by local disruption of the cortex by laser ablation (Sedzinski et al., 2011). However, it is not fully clear what defines the sites of bleb initiation in the absence

Chikina et al.
Structure of actin cortex in membrane blebs

Journal of Cell Biology   446
https://doi.org/10.1083/jcb.201806075
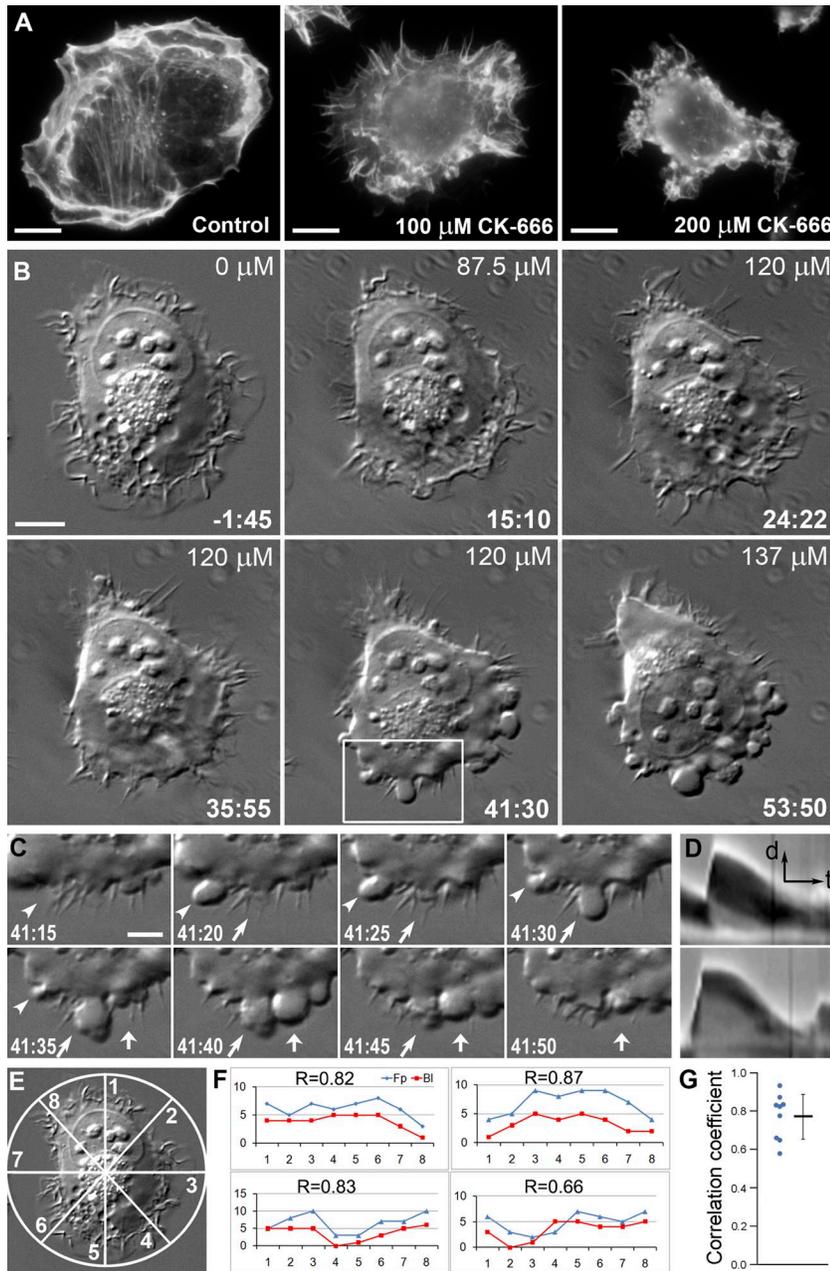
Figure 1. **Transition from lamellipodia to blebbing in CK-666–treated HT1080 cells includes a filopodial stage. (A)** Phalloidin staining in indicated conditions. **(B)** Time-lapse DIC imaging of an HT1080 cell exposed to increasing CK-666 concentrations. Time is in minutes:seconds relative to the first addition of CK-666 at 87.5 µM. The CK-666 concentration was increased to 120 µM at t = 24:22 and to 137 µM at t = 51:44. **(C)** Bleb dynamics from the boxed region in B at higher time resolution. Individual blebs are marked by arrows and arrowheads. CK-666 concentration during this time period was 120 µM. **(D)** Representative kymographs of bleb dynamics with (bottom) and without (top) a stationary phase. Arrows indicate time (t) and protrusion direction (d). Scale bars: 10 µm (A and B), 5 µm (C), 2 µm (D, d arrow), and 30 s (D, t arrow). See also Video 1. **(E)** Diagram illustrating a method to quantify distribution of protrusion. Numbers of blebs and filopodia were determined in each of the eight sectors of the cell perimeter. **(F)** Representative four graphs showing the numbers of blebs (Bl) or filopodia (Fp; y axis) versus the sector number (x axis). Pearson correlation coefficient (r) is shown for each graph. Upper left graph corresponds to the cell shown in B. **(G)** Distribution of individual r values (left) with mean ± SD (right) for n = 9 cells; P <0.0001 relative to r = 0 (two-tailed t test).

of experimental intervention and how these sites could be related to filopodia. It has been proposed that the concave cell surface at the filopodium base favors the outward-directed membrane tension, membrane detachment, and thus bleb formation (Tyson et al., 2014). However, this idea does not exclude a possibility that a particular organization of the juxtafilopodial cytoskeleton can also favor bleb initiation.

In PREM images, the actin cytoskeleton of control HT1080 cells could be roughly subdivided into peripheral actin-rich protrusions and the cortex over the cell body (Fig. 2 A). The cortex was formed by a nonoriented actin network, which was slightly sparser at the junction with the dense branched actin network in lamellipodia and ruffles at the cell periphery. Although typical filopodia were rare in this cell type, the related structures (microspikes) were occasionally present at the leading edge of

HT1080 cells, as indicated by the presence of parallel actin bundles traversing the lamellipodial network. Notably, the lamellipodial actin network often appeared sparser around the roots of these bundles (Fig. 2 B and Fig. S2, A and B). This visual impression was confirmed by quantitative evaluation of cytoskeleton densities in PREM images, which showed that an average cytoskeleton density in the regions encompassing filopodial roots was significantly (P < 0.0001) decreased by ~15%, as compared with the adjacent lamellipodial regions (Fig. 2 C).

For PREM analysis of cells with filopodial and blebbing phenotypes, we used cultures treated with 200 µM CK-666, as they contained both cell types. Cells with a filopodial phenotype had greatly diminished amounts of branched actin network at the cell periphery, although some miniscule lamellipodia remained (Fig. 2 D). The dorsal cortex in such cells remained dense, whereas
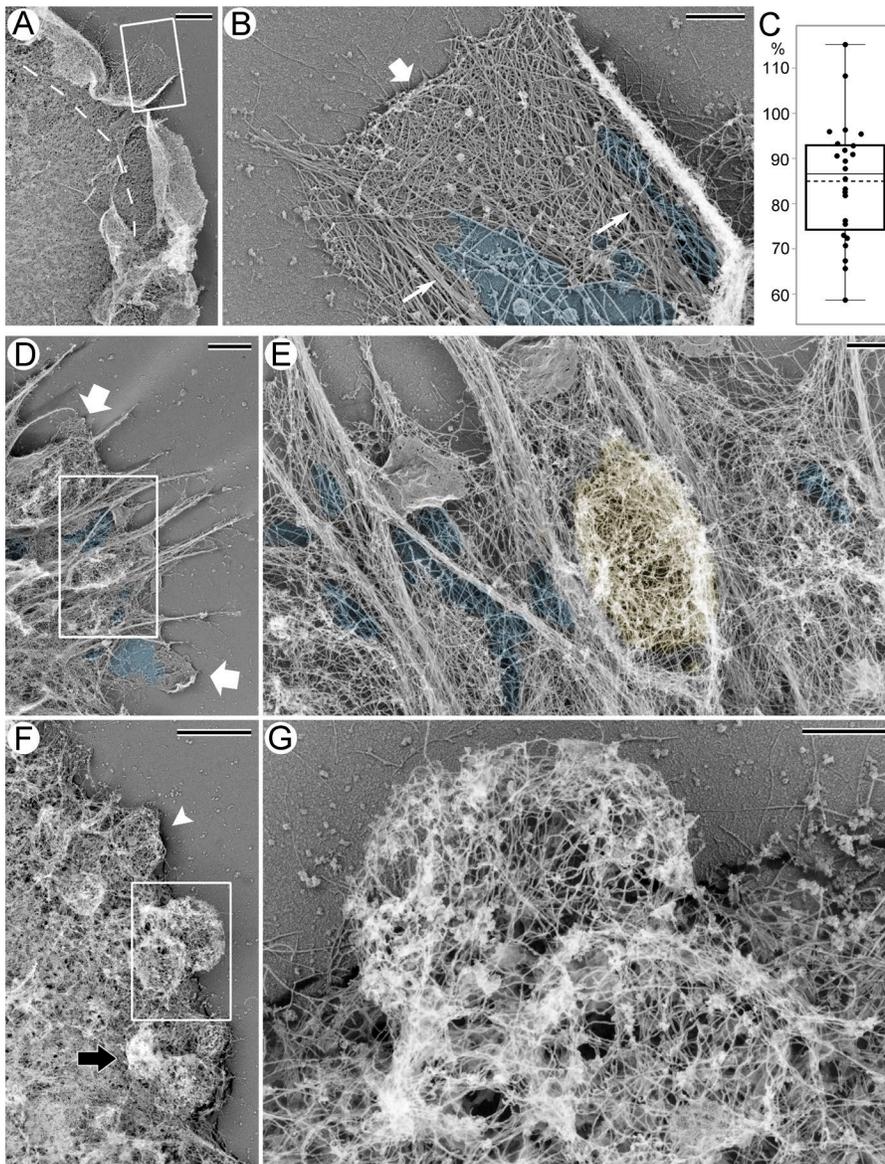
Figure 2. **PREM of HT1080 cells with and without CK-666 treatment. (A)** Peripheral region of a control cell; dashed line marks the approximate boundary between protrusions containing branched actin networks and the cell body associated with other types of actin filament arrays. Boxed region is enlarged and rotated counterclockwise in B. **(B)** Lamellipodium (wide arrow) with embedded filopodia (thin arrows). Sparse cytoskeleton near filopodial bundles is highlighted in blue. **(C)** Relative cytoskeleton densities around filopodial roots expressed as percentage of the cytoskeleton density in adjacent lamellipodial regions in the same image (85 ± 13%; mean ± SD; P <0.0001; paired two-tailed t test; distribution normality was confirmed by Kolmogorov–Smirnov test; n = 24 region pairs). Box and whiskers encompass 50% and 100% of data, respectively. Thin line in the box indicates median, dashed line indicates mean. **(D–G)** Peripheral regions of cells treated with 200 µM CK-666 with filopodial (D and E) or blebbing (F and G) phenotype. **(D)** Wide arrows mark remaining lamellipodia. Boxed region is enlarged and rotated counterclockwise in E. **(E)** Yellow color marks a bleb formed between filopodial roots, as confirmed by 3D views of this region (not shown). Blue shade in D and E marks sparse cytoskeleton. **(F)** White arrowhead marks a bleb filled with a relatively uniform network. Stereo view of this bleb is shown in Fig. S1 D. Black arrow marks a crumpled bleb. Boxed region is enlarged and rotated counterclockwise in G. **(G)** Rounded blebs with a dense cortical cytoskeleton and a sparser internal network. An animated tilt series of this bleb is shown in Video 2. Scale bars: 2 µm (A, D, and F) and 500 nm (B, E, and G). See also Fig. S2.

the actin network at the filopodial bases and behind the remaining lamellipodia became notably sparser (Fig. 2, D and E). These exaggerated gaps appeared to be suitable sites for the bleb formation. Indeed, occasional blebs observed in cells with the filopodial phenotype were usually located at or between filopodia (Fig. 2 E).

Our PREM results suggest a structural basis for the preferential formation of blebs near filopodia. Specifically, blebs can form at the filopodial bases because these regions appear to be the weakest parts of the cytoskeleton even in control conditions, and this apparent weakness is exacerbated after Arp2/3 complex inhibition. Our findings, however, do not imply that filopodia are absolutely necessary for bleb formation. Rather, filopodia in our experimental system serve as convenient markers to correlate the sites of bleb formation with the structure of the preexisting cytoskeleton. In other cells and/or conditions, comparable cytoskeleton weaknesses could exist at different locations but nonetheless serve as vulnerable sites for bleb initiation under conditions of high contraction. For example, a reduced density of the cytoskeletal network that is frequently observed at the boundary between lamellipodia and

lamellae (Svitkina et al., 1984) may predispose these regions to bleb initiation in cells lacking filopodia. Consistent with this idea, when a cell was induced to switch acutely from lamellipodia to blebbing, the blebs were found to appear at the same subcellular location as lamellipodia (Bergert et al., 2012). On the other hand, local cytoskeleton weaknesses are not sufficient for bleb initiation and only define preferential sites for the formation of blebs if they are induced by high cellular contractility.

Structural categories of the bleb cytoskeleton revealed by PREM

In cells with a blebbing phenotype, blebs were preferentially found at the cell leading edge, as compared with the dorsal cell surface (Fig. 2, F and G; and Fig. S2, C–I). In general, the actin cytoskeleton in blebs consisted of long actin filaments organized into complex networks. Based on their cytoskeletal organization, blebs could be categorized into several types. In the most conspicuous blebs that represented almost half of the bleb population (46.5%; n = 71 blebs from two independent experiments), the
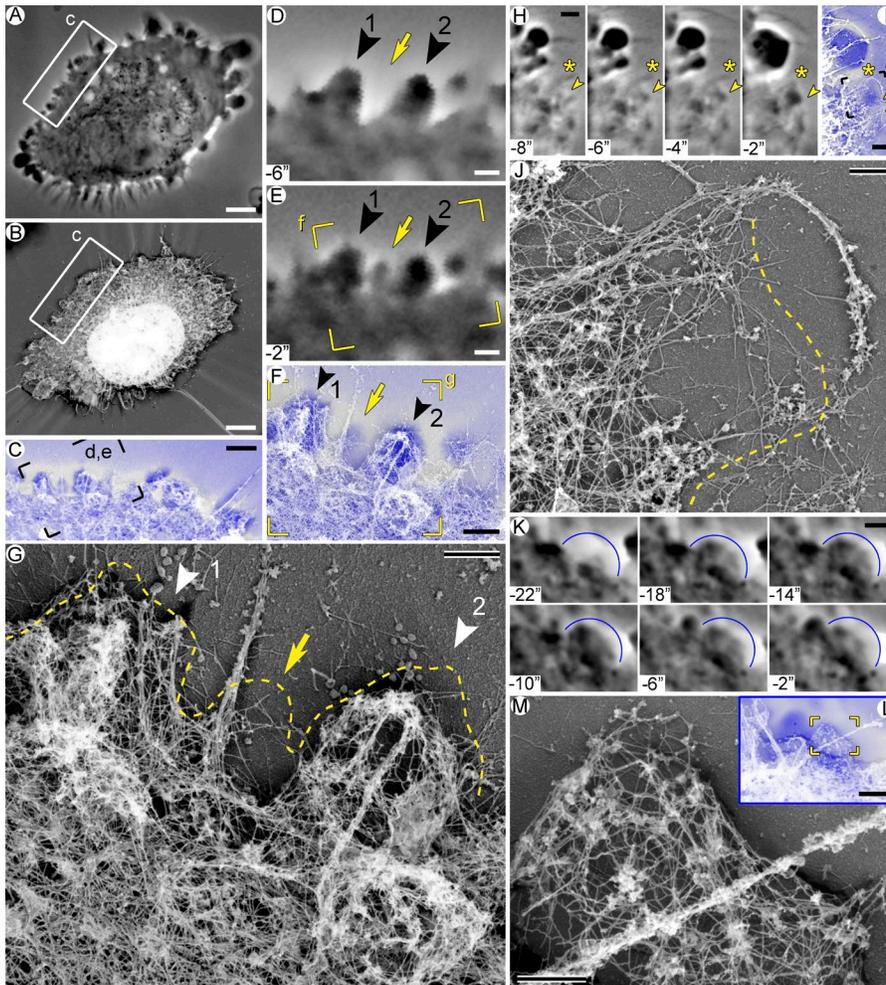
Figure 3. **Actin cytoskeleton at different stages of the bleb life cycle.** Correlative video and PREM of blebbing HT1080 cells treated with 200 µM CK-666. **(A–G)** Cell #1. **(A)** Last phase-contrast image before extraction at t = 0. **(B)** PREM of the same cell. **(C)** Overlay of boxed regions from A (blue) and B (gray). **(D and E)** Time-lapse images from the framed region in C showing formation of a nascent bleb (arrow) and two retracting blebs (arrowheads). Both retracting blebs emerged at t = –64 s and finished expansion at t = –20 s, but bleb 1 began retracting earlier (at t = –12 s) than bleb 2 (at t = –4 s). **(F)** Overlay of the framed region in E (blue) and corresponding PREM image (gray). **(G)** PREM of the framed region in F; dashed line marks the cell contour from the phase-contrast image. **(H–J)** Cell #2. **(H)** Time-lapse images showing an expanding bleb (arrowheads); asterisks mark an adjacent filopodium. **(I)** Overlay of the last video frame (blue) and the corresponding PREM image (gray). **(J)** PREM of the framed region in I. Dashed line indicates the contour of the bleb labeled in H and I. **(K–M)** Cell #3. **(K)** Time-lapse images of a bleb (blue arc) fixed at a stationary/early retraction phase. The bleb emerged at t = –22 s, reached maximal size at t = –18 s, and underwent minor retraction between t = –6 and –2 s. **(L)** Overlay of the last video frame (blue) and the corresponding PREM image (gray). **(M)** PREM of the framed region in L. Scale bars: 5 µm (A and B), 2 µm (C, H, I, K, and L), 1 µm (D–F), and 500 nm (G, J, and M). Time in seconds before extraction. See also Fig. S3 and Video 3.

actin network was relatively dense at the cortical region (Figs. 2 G and S2). However, it also extended from the bleb periphery into its interior, as can be seen from stereo-pair images (Fig. S2) and animated series of tilt images (Video 2). Thus, the bleb's cytoskeleton not only consists of a thin submembrane cortex, as it is usually assumed, but also represents an intricate 3D structure that fills the bleb volume and includes both a denser peripheral cortex and a sparser cross-linked internal network. The internal actin filaments in blebs could previously escape detection by fluorescence microscopy, because they are sparse and poorly organized. Therefore, the fluorescence signal produced by these filaments is expected to be too weak and poorly structured to allow for its reliable discrimination from the background fluorescence. In a small fraction of blebs (5.6%), the actin network was generally sparse and mostly consisted of actin filaments entering from the cell body into the basal part of the bleb, whereas only a few filaments could be seen at the distal bleb margin (Fig. S2 C). These cases might correspond to an early stage of cytoskeleton assembly in the bleb. The third type of blebs (11.3%) contained an actin network of moderate density with no significant enrichments either at the base or at the cortex (Fig. S2, D, upper left bleb; F, right bleb; and G, two central blebs). Finally, 36.6% of blebs, which likely corresponded to retracting blebs, were characterized by irregular shapes and a very dense cytoskeleton (Fig. S2, D, lower right

bleb; and G and I, upper bleb). These data suggest that the bleb cytoskeleton undergoes reorganization during a bleb's lifetime.

Time-resolved structural remodeling of the bleb cortex
The observed range of cytoskeletal architectures could correspond to distinct stages of the bleb life cycle. To determine the cytoskeleton organization in blebs with known life history, we used correlative video microscopy and PREM (Fig. 3 and Video 3). HT1080 cells were pretreated with 200 µM CK-666 and, after short-term imaging by phase-contrast microscopy, extracted, fixed, and processed for PREM. Although these poorly attached cells often shrank during extraction, PREM and phase-contrast images could be reliably matched for individual segments of the cell periphery (Fig. 3, A–C). Using this approach, we analyzed in detail 87 blebs (32 expanding and 55 retracting) from four cells.

Within nascent blebs (Fig. 3, A–G, arrow; and Fig. S3, G and J), we could not reliably detect cytoskeletal structures in the corresponding regions by PREM, consistent with the idea that blebs lack prominent cytoskeleton at this stage (Charras et al., 2006). Similar to our light microscopy observations, nascent blebs often emerged at the filopodial bases where prominent gaps in the actin network could be seen (Fig. 3 G and Fig. S3, C and J), supporting the idea that voids in the cytoskeletal networks at filopodial bases facilitate bleb initiation.

At slightly later stages of bleb expansion (Fig. 3, H–J; and Fig. S3 C), sparse actin filaments could be already observed in the bleb. This emerging cytoskeleton was typically denser at the bleb base and largely consisted of actin filaments that entered the bleb through its base. Additional sparse filaments were present cortically at the distal bleb margin (Fig. 3 J). This cytoskeletal organization resembles the respective category of blebs in noncorrelative PREM images and suggests that the initial assembly of the bleb cytoskeleton largely results from elongation of preexisting filaments at the bleb base with lesser contribution from actin nucleation at the bleb membrane. Regrowth of actin filaments through the bleb neck could not be detected previously (Bovellan et al., 2014), possibly because of lower sensitivity of fluorescence microscopy or because later stages of the bleb life cycle were analyzed.

In fully expanded blebs at the stationary/slow retraction phase (Fig. 3, K–M), actin filaments in the form of a loose 3D network filled the bleb without obvious enrichments at the bleb base or cortex (Fig. 3 M and Fig. S3, H and M). At the beginning of fast retraction, when blebs still retained a smooth roundish shape, the cortical layer became noticeably denser than the internal actin network that appeared to integrate different regions of the bleb cortex (Fig. 3 G, bleb 2; and Fig. S3, H and M). The cortical layer of the bleb cytoskeleton at this stage consisted of an irregular actin network of long filaments that had roughly similar density around the bleb perimeter with no obvious enrichment at the bleb base or tip. This architecture corresponds to the most conspicuous type of blebs in noncorrelative images (Fig. 2, F and G). These data suggest that the process of cytoskeleton reassembly in blebs increasingly involves cortical nucleation of actin filaments. Close examination of the bleb cortex at this stage revealed that it contained regions of higher density and occasional loose bundles on the background of a sparser actin network. Small sparse bundles were also found at the base of blebs. These local densities likely reflect local contractions within the bleb. The correlation between the beginning of the active bleb retraction and an increased density of the bleb cortex suggests that retraction starts when the actin cytoskeleton inside the bleb, especially the cortex, reaches a critical mass.

At the late stages of bleb retraction, when blebs looked crumpled by light microscopy (Fig. 1 C), PREM data showed that the bleb cortex exhibited large folds and ridges made of dense actin networks and bundles (Fig. 3 G, bleb 1; and Fig. S3, D and E). We suggest that a crumpled shape of retracting blebs results from nonuniform contraction of the stochastically organized bleb cytoskeleton, which is attached to the membrane at intermittent sites. The internal actin filament network can significantly contribute to the wrinkled shape of retracting blebs, because it seems to be better positioned to pull the membrane inward, as compared with more tangentially oriented contractile force expected from the cortical layer. In this scenario, the internal actin network would induce local invaginations of the bleb surface and help faster retraction, whereas the bleb cortex may ensure more balanced bleb shrinkage and prevent membrane rupture.

Organization of nonmuscle myosin II in blebs

We next used immunogold PREM to determine organization of nonmuscle myosin II (NMII) in blebs (Figs. 4 and S4). For this

purpose, we used an antibody that does not discriminate individual NMII isoforms. We found that NMII was consistently present in association with actin filaments in blebs of different morphologies. Specifically, NMII immunogold was found in early-stage blebs, which are characterized by a relatively sparse cytoskeleton either evenly distributed or enriched at the base (Figs. 4 B and S4 B), in the middle-stage blebs with a cortically enriched cytoskeleton (Figs. 4 F and S4 D), and in the late-stage blebs with a crumpled shape and dense cytoskeleton inside. In all these cases, NMII immunogold particles can be seen at both the base and the tip of the bleb. Moreover, gold particles can be associated not only with cortical actin filaments but also with actin filaments in the bleb interior (Figs. 4 D and S4 D). These data suggest that NMII arrives early during assembly of the bleb cytoskeleton and can mediate contraction both within the cortical layer and pull onto the cortex from inside.

Conclusions

Using correlative video and PREM analysis of blebbing HT1080 cells, we reveal endogenous sites for preferential bleb initiation and characterize the assembly and reorganization of the bleb cytoskeleton during the bleb life cycle (Fig. 5). Specifically, we show that a switch from lamellipodia to blebs after inhibition of the Arp2/3 complex includes an intermediate stage of filopodia formation and that sites of bleb initiation are biased toward filopodial bases, where the sparser cytoskeleton produces vulnerable sites for plasma membrane inflation by intracellular pressure (Fig. 5, A–C). These data establish that intrinsic local weaknesses of the cytoskeleton are predisposed to bleb formation. This concept also likely applies to constitutively blebbing cells, in which new blebs frequently emerge from the tip of an existing bleb. We speculate that these "mother" blebs are likely at the early stage of their cycle, at which the cytoskeleton is sparser at the tip than at the base of the bleb (Fig. 5 D).

Reassembly of the cytoskeleton in the initially "empty" blebs begins while they are still expanding. Many actin filaments at this stage enter the bleb from the cell body, while nucleation of new actin filaments at the bleb membrane is limited at this stage (Fig. 5 D). At the stationary/slow retraction stage, the bleb cytoskeleton becomes more isotropic, probably signifying a greater contribution of de novo nucleation at the membrane (Fig. 5 E). This cortical nucleation apparently leads to the formation of a dense cortex integrated with the sparser internal network in the bleb, which correlates with the onset of fast bleb retraction (Fig. 5 F). As retraction proceeds, the bleb cortex develops wrinkles and locally contracted regions (Fig. 5 G), likely produced by contraction of both cortical and internal components of the bleb cytoskeleton, as suggested by the presence of NMII in both components of the bleb cytoskeleton.

Materials and methods

Cell culture and treatments

HT1080 fibrosarcoma human cells (ATCC) were cultured in DMEM with 10% fetal bovine serum (HyClone) and 1% penicillin/streptomycin (Quality Biological) and maintained at 37°C (humidified, in 5% CO_2). For phalloidin staining, cells were plated

Chikina et al.
Structure of actin cortex in membrane blebs

Journal of Cell Biology
https://doi.org/10.1083/jcb.201806075

450
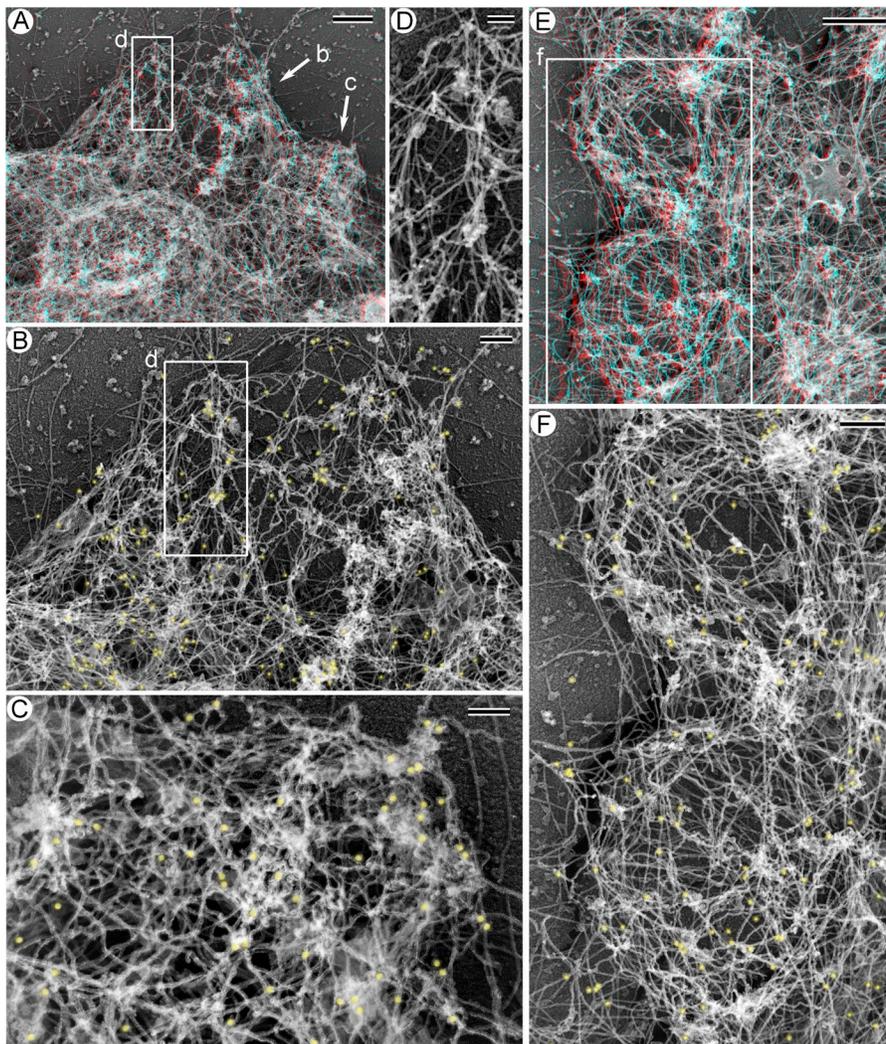
Figure 4. **NMII is associated with the bleb cytoskeleton in different types of blebs.** Immunogold PREM of blebbing HT1080 cells treated with 200 µM CK-666. **(A and E)** Anaglyph stereo images of blebs at the cell periphery. **(B and C)** Enlarged 2D images of an early-stage bleb (B) and a late-stage bleb (C) from A. Immunogold particles are pseudocolored yellow. **(D)** A small actin filament bundle in the bleb interior from the boxed region in A and B shown in 2D without pseudocolor. As can be appreciated from A, this NMII-associated bundle ascends from its tip (at the top of the image) toward the base (at the bottom of the image), while NMII immunogold particles associated with the bundle are located inside the bleb. **(F)** Two middle-stage blebs with cortical enrichment of the cytoskeleton enlarged from E shown as a 2D image with NMII immunogold pseudolcolored yellow. Scale bars: 500 nm (A and E), 200 nm (B and F), and 100 nm (C and D).

on glass coverslips, allowed to spread for 12–16 h, fixed with 3.7% formaldehyde in PBS at 37°C for 10 min, washed three times with PBS, permeabilized with 0.1% Triton X-100 in PBS for 2 min, and stained with phalloidin–Alexa Fluor 488 (Invitrogen). For drug treatment, CK-666 (Tocris Bioscience) was added for 1 h at final concentrations of 100 or 200 µM prepared from a 100-mM stock solution in DMSO. An equivalent amount of DMSO was added to control dishes. For live-cell imaging by differential interference contrast (DIC) microscopy, cells were cultured in glass-bottom dishes for 12–16 h before the start of imaging. After a period of imaging without an inhibitor, CK-666 was added stepwise to a culture dish on the microscope stage during time-lapse imaging. At the first step, 500 µl of 350 µM CK-666 in culture medium was added to the dish containing cells in 1.5 ml medium to obtain 87.5 µM CK-666 in a total volume of 2 ml; at the second step, 500 µl of 250 µM CK-666 in medium was added to the same dish to obtain 120 µM CK-666 in a total volume of 2.5 ml; and at the third step, 500 µl of 220 µM CK-666 in medium was added to the dish to obtain 137 µM CK-666 in a total volume of 3 ml. For CK-666 washout, 50% of the drug-containing culture medium was removed and replaced with an equivalent amount of a drug-free medium. This procedure was repeated nine times

with serum-free medium and then five times with serum-containing medium before continuation of imaging. Experiments with 25 µM CK-869 (C9124; Sigma) and 100 µM CK-689 (182517; Sigma) were performed in a similar manner, except that a single concentration was used for each drug. For correlative PREM, cells were cultured in homemade glass-bottom dishes with fiducial marks (Svitkina, 2016) for 12–16 h and pretreated with 200 µM CK-666 for 1 h before starting time-lapse imaging.

Light microscopy

Fluorescence microscopy was performed using Zeiss Axioplan microscope equipped with Plan-Neofluar 100×/1.30 NA oil and Plan-Neofluar 40×/0.75 NA objectives and an Olympus DP 70 camera driven by DP Controller software. DIC microscopy was performed using Nikon Eclipse Ti-E microscope equipped with Plan Fluor 40×/1.30 NA oil objective and Hamamatsu ORCA-ERC 4742–80 camera driven by NIS-Elements AR software (Nikon). Time-lapse sequences were acquired at 5-s intervals. For stepwise addition of CK-666, time-lapse sequences were temporarily stopped. Phase-contrast microscopy for correlative PREM analyses was performed using Eclipse TE2000-U inverted microscope (Nikon) equipped with Plan Apo 100×/1.3 NA objective and
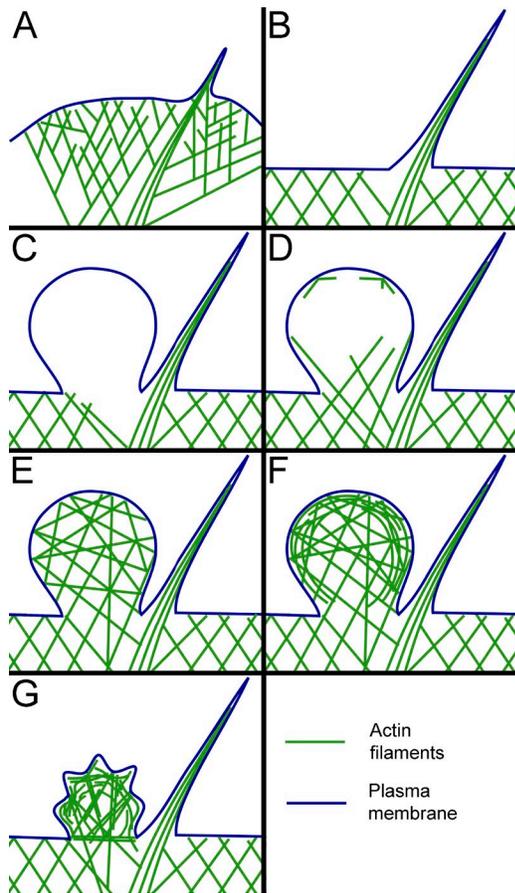
Figure 5. Cytoskeleton assembly and remodeling during bleb's life cycle. (A) Branched actin network in lamellipodia with an embedded filopodial bundle. Cytoskeletal network is sparser around the filopodial root. **(B)** Transitional filopodial stage that precedes the initiation of blebbing. Branched network is suppressed and juxtafilopodial gaps are more prominent. **(C)** Nascent bleb formed at the filopodial base lacks detectable cytoskeletal filaments. **(D)** Expanding bleb contains actin filaments invading through the neck from the cell body. Some filaments are also nucleated at the bleb margins. **(E)** Fully expanded bleb at the stationary/slow retraction phase. Actin filaments form a relatively isotropic network within the bleb. **(F)** A bleb at the beginning of fast retraction contains cortically enriched cytoskeleton integrated with the sparser internal network. **(G)** A crumpled bleb during advanced retraction. Membrane folds can be produced by radially oriented pulling force from end-on anchored actin filaments, whereas overall shrinkage could result from contractile activity of tangentially oriented cortical filaments.

Cascade 512B CCD camera (Photometrics) driven by MetaMorph software (Molecular Devices). Time-lapse sequences were acquired at 2-s intervals. Kymographs for determination of parameters of bleb kinetics were prepared and analyzed using ImageJ and Microsoft Excel software.

PREM

Detailed procedures for regular and correlative PREM have been described previously (Svitkina, 2016). Briefly, cells grown on coverslips (for regular PREM) or in glass-bottom dishes (for correlative PREM) were quickly extracted for 2–3 min at room temperature with 1% Triton X-100 in PEM buffer (100 mM Pipes-KOH, pH 6.9, 1 mM MgCl2, and 1 mM EGTA) and 2 µM unlabeled

phalloidin. For correlative PREM, extraction solution was added to the dish on a microscope stage. After three quick rinses with PEM buffer containing 2 µM unlabeled phalloidin, extracted cells were fixed with 2% glutaraldehyde in 0.1 M sodium cacodylate buffer, pH 7.3, for 20 min. Immunogold staining of NMII was performed essentially as described previously (Svitkina, 2016). Briefly, cells were extracted as described above, rinsed with PEM buffer, and incubated without fixation for 20 min at room temperature with primary rabbit antibody against NMII (BT-564; Biomedical Technologies) diluted 1:20 in PEM buffer containing 4 µM unlabeled phalloidin. Then, samples were washed with PEM, fixed for 20 min with 0.2% glutaraldehyde, washed with PBS, quenched with NaBH4, and incubated overnight with a secondary antibody conjugated with 18 nm colloidal gold (705-205-147; Jackson ImmunoResearch) at 1:5 dilution and then washed and fixed with 2% glutaraldehyde.

After glutaraldehyde fixation, samples were then sequentially fixed with 1 mg/ml aqueous tannic acid and 2 mg/ml aqueous uranyl acetate, critical point dried, rotary shadowed with platinum at ~45° and carbon at ~90°, transferred onto electron microscopic grids, and analyzed using a JEM 1011 transmission electron microscope (JEOL) operated at 100 kV. Images were captured with ORIUS 832.10W CCD camera (Gatan) and presented in inverted contrast. Stereo pairs were acquired at ±10° tilt angles and combined into a red-cyan anaglyph image using Adobe Photoshop software. Use red-cyan anaglyph glasses with red filter over the right eye to visualize a stereo image. Light microscopy and PREM images were aligned using Adobe Photoshop.

Data analyses

Analysis of bleb initiation sites relative to filopodia was performed using time-lapse movies of cells treated with 200 µM CK-666. Only blebs formed at the cell edges without preexisting blebs were included in quantifications. For quantification of distribution of filopodia and blebs along the cell perimeter, a circle circumscribing the cell was divided into eight equal sectors, as shown in Fig. 1 C. The number of filopodia and newly formed blebs for each sector was determined using time-lapse sequences of CK-666–treated cells. Only new blebs formed at the previously nonblebbing cell edges were included in quantification, whereas secondary blebs formed from preexisting blebs or at the sites of retracted blebs were excluded from the analysis. The number of filopodia was estimated using the last time frame before initiation of blebbing. The correlation coefficient (r) between the numbers of blebs and filopodia in the sectors the cell perimeter was determined using CORREL function in Microsoft Excel. The statistical significance of r relative to the null hypothesis ($r = 0$) was determined by a two-tailed t test after confirming Gaussian distribution of data by a Kolmogorov–Smirnov test using GraphPad Instat software.

Local cytoskeleton densities were determined using PREM images, which showed relatively flat regions of lamellipodia with embedded filopodial bundles and did not contain ruffles or other bright 3D structures. Mean gray intensity levels were determined after background subtraction within circular regions

(0.2–2.0 μm²) using ImageJ (Fiji) software. The mean intensities were compared pairwise between a region encompassing the filopodial root with the surrounding cytoskeleton and an identical region located in the immediately adjacent lamellipodium. Statistical analysis was performed by two-tailed paired *t* test using GraphPad Instat software.

Online supplemental material

Fig. S1 shows protrusive activity of HT1080 cells after CK-666 washout and after treatment with 25 μM CK-869 or 100 μM CK-689. Fig. S2 shows 3D PREM images of different protrusive structures in HT1080 cells. Fig. S3 shows additional examples of correlative PREM of blebs induced by CK-666 in HT1080 cells. Fig. S4 shows immunogold staining of NMII in different types of blebs. Video 1 shows protrusive activity of the HT1080 cell shown in Fig. 1 in response to increasing concentrations of CK-666. Video 2 shows an animated tilt series of PREM images of the blebs shown in Fig. 2 G. Video 3 shows blebbing activity of cell #1 used for correlative PREM in Fig. 3.

References

Aoki, K., F. Maeda, T. Nagasako, Y. Mochizuki, S. Uchida, and J. Ikenouchi. 2016. A RhoA and Rnd3 cycle regulates actin reassembly during membrane blebbing. *Proc. Natl. Acad. Sci. USA.* 113:E1863–E1871. https://doi.org/10.1073/pnas.1600968113

Beckham, Y., R.J. Vasquez, J. Stricker, K. Sayegh, C. Campillo, and M.L. Gardel. 2014. Arp2/3 inhibition induces amoeboid-like protrusions in MCF10A epithelial cells by reduced cytoskeletal-membrane coupling and focal adhesion assembly. *PLoS One.* 9:e100943. https://doi.org/10.1371/journal.pone.0100943

Bergert, M., S.D. Chandradoss, R.A. Desai, and E. Paluch. 2012. Cell mechanics control rapid transitions between blebs and lamellipodia during migration. *Proc. Natl. Acad. Sci. USA.* 109:14434–14439. https://doi.org/10.1073/pnas.1207968109

Bergert, M., A. Erzberger, R.A. Desai, I.M. Aspalter, A.C. Oates, G. Charras, G. Salbreux, and E.K. Paluch. 2015. Force transmission during adhesion-independent migration. *Nat. Cell Biol.* 17:524–529. https://doi.org/10.1038/ncb3134

Bovellan, M., Y. Romeo, M. Biro, A. Boden, P. Chugh, A. Yonis, M. Vaghela, M. Fritzsche, D. Moulding, R. Thorogate, et al. 2014. Cellular control of cortical actin nucleation. *Curr. Biol.* 24:1628–1635. https://doi.org/10.1016/j.cub.2014.05.069

Burke, T.A., J.R. Christensen, E. Barone, C. Suarez, V. Sirotkin, and D.R. Kovar. 2014. Homeostatic actin cytoskeleton networks are regulated by assembly factor competition for monomers. *Curr. Biol.* 24:579–585. https://doi.org/10.1016/j.cub.2014.01.072

Charras, G., and E. Paluch. 2008. Blebs lead the way: how to migrate without lamellipodia. *Nat. Rev. Mol. Cell Biol.* 9:730–736. https://doi.org/10.1038/nrm2453

Charras, G.T., J.C. Yarrow, M.A. Horton, L. Mahadevan, and T.J. Mitchison. 2005. Non-equilibration of hydrostatic pressure in blebbing cells. *Nature.* 435:365–369. https://doi.org/10.1038/nature03550

Charras, G.T., C.K. Hu, M. Coughlin, and T.J. Mitchison. 2006. Reassembly of contractile actin cortex in cell blebs. *J. Cell Biol.* 175:477–490. https://doi.org/10.1083/jcb.200602085

Charras, G.T., M. Coughlin, T.J. Mitchison, and L. Mahadevan. 2008. Life and times of a cellular bleb. *Biophys. J.* 94:1836–1853. https://doi.org/10.1529/biophysj.107.113605

Chugh, P., and E.K. Paluch. 2018. The actin cortex at a glance. *J. Cell Sci.* 131:jcs186254. https://doi.org/10.1242/jcs.186254

Chugh, P., A.G. Clark, M.B. Smith, D.A.D. Cassani, K. Dierkes, A. Ragab, P.P. Roux, G. Charras, G. Salbreux, and E.K. Paluch. 2017. Actin cortex architecture regulates cell surface tension. *Nat. Cell Biol.* 19:689–697. https://doi.org/10.1038/ncb3525

Cunningham, C.C. 1995. Actin polymerization and intracellular solvent flow in cell surface blebbing. *J. Cell Biol.* 129:1589–1599. https://doi.org/10.1083/jcb.129.6.1589

Davidson, A.J., C. Amato, P.A. Thomason, and R.H. Insall. 2018. WASP family proteins and formins compete in pseudopod- and bleb-based migration. *J. Cell Biol.* 217:701–714. https://doi.org/10.1083/jcb.201705160

Derivery, E., J. Fink, D. Martin, A. Houdusse, M. Piel, T.E. Stradal, D. Louvard, and A. Gautreau. 2008. Free Brick1 is a trimeric precursor in the assembly of a functional wave complex. *PLoS One.* 3:e2462. https://doi.org/10.1371/journal.pone.0002462

Eghiaian, F., A. Rigato, and S. Scheuring. 2015. Structural, mechanical, and dynamical variability of the actin cortex in living cells. *Biophys. J.* 108:1330–1340. https://doi.org/10.1016/j.bpj.2015.01.016

Friedl, P., and K. Wolf. 2003. Tumour-cell invasion and migration: diversity and escape mechanisms. *Nat. Rev. Cancer.* 3:362–374. https://doi.org/10.1038/nrc1075

Fujiwara, T.K., K. Iwasawa, Z. Kalay, T.A. Tsunoyama, Y. Watanabe, Y.M. Umemura, H. Murakoshi, K.G. Suzuki, Y.L. Nemoto, N. Morone, and A. Kusumi. 2016. Confined diffusion of transmembrane proteins and lipids induced by the same actin meshwork lining the plasma membrane. *Mol. Biol. Cell.* 27:1101–1119. https://doi.org/10.1091/mbc.E15-04-0186

Gomez, T.S., K. Kumar, R.B. Medeiros, Y. Shimizu, P.J. Leibson, and D.D. Billadeau. 2007. Formins regulate the actin-related protein 2/3 complex-independent polarization of the centrosome to the immunological synapse. *Immunity.* 26:177–190. https://doi.org/10.1016/j.immuni.2007.01.008

Goudarzi, M., K. Tarbashevich, K. Mildner, I. Begemann, J. Garcia, A. Paksa, M. Reichman-Fried, H. Mahabaleshwar, H. Blaser, J. Hartwig, et al. 2017. Bleb expansion in migrating cells depends on supply of membrane from cell surface invaginations. *Dev. Cell.* 43:577–587.e5. https://doi.org/10.1016/j.devcel.2017.10.030

Jiao, M., D. Wu, and Q. Wei. 2018. Myosin II-interacting guanine nucleotide exchange factor promotes bleb retraction via stimulating cortex reassembly at the bleb membrane. *Mol. Biol. Cell.* 29:643–656. https://doi.org/10.1091/mbc.E17-10-0579

Lämmermann, T., and M. Sixt. 2009. Mechanical modes of 'amoeboid' cell migration. *Curr. Opin. Cell Biol.* 21:636–644. https://doi.org/10.1016/j.ceb.2009.05.003

Laser-Azogui, A., T. Diamant-Levi, S. Israeli, Y. Roytman, and I. Tsarfaty. 2014. Met-induced membrane blebbing leads to amoeboid cell motility and invasion. *Oncogene.* 33:1788–1798. https://doi.org/10.1038/onc.2013.138

Liu, Y.J., M. Le Berre, F. Lautenschlaeger, P. Maiuri, A. Callan-Jones, M. Heuzé, T. Takaki, R. Voituriez, and M. Piel. 2015. Confinement and low adhesion induce fast amoeboid migration of slow mesenchymal cells. *Cell.* 160:659–672. https://doi.org/10.1016/j.cell.2015.01.007

Ma, M., and M. Baumgartner. 2013. Filopodia and membrane blebs drive efficient matrix invasion of macrophages transformed by the intracellular parasite Theileria annulata. *PLoS One.* 8:e75577. https://doi.org/10.1371/journal.pone.0075577

Maugis, B., J. Brugués, P. Nassoy, N. Guillen, P. Sens, and F. Amblard. 2010. Dynamic instability of the intracellular pressure drives bleb-based motility. *J. Cell Sci.* 123:3884–3892. https://doi.org/10.1242/jcs.065672

Meyen, D., K. Tarbashevich, T.U. Banisch, C. Wittwer, M. Reichman-Fried, B. Maugis, C. Grimaldi, E.M. Messerschmidt, and E. Raz. 2015. Dynamic filopodia are required for chemokine-dependent intracellular polarization during guided cell migration in vivo. *eLife.* 4:e05279. https://doi.org/10.7554/eLife.05279

Nolen, B.J., N. Tomasevic, A. Russell, D.W. Pierce, Z. Jia, C.D. McCormick, J. Hartman, R. Sakowicz, and T.D. Pollard. 2009. Characterization of two classes of small molecule inhibitors of Arp2/3 complex. *Nature.* 460:1031–1034. https://doi.org/10.1038/nature08231

Paluch, E.K., and E. Raz. 2013. The role and regulation of blebs in cell migration. *Curr. Opin. Cell Biol.* 25:582–590. https://doi.org/10.1016/j.ceb.2013.05.005

Petrie, R.J., and K.M. Yamada. 2015. Fibroblasts lead the way: A unified view of 3D cell motility. *Trends Cell Biol.* 25:666–674. https://doi.org/10.1016/j.tcb.2015.07.013

Rentsch, P.S., and H. Keller. 2000. Suction pressure can induce uncoupling of the plasma membrane from cortical actin. *Eur. J. Cell Biol.* 79:975–981. https://doi.org/10.1078/0171-9335-00124

Ruprecht, V., S. Wieser, A. Callan-Jones, M. Smutny, H. Morita, K. Sako, V. Barone, M. Ritsch-Marte, M. Sixt, R. Voituriez, and C.P. Heisenberg. 2015. Cortical contractility triggers a stochastic switch to fast amoeboid cell motility. *Cell.* 160:673–685. https://doi.org/10.1016/j.cell.2015.01.008

Sahai, E., and C.J. Marshall. 2003. Differing modes of tumour cell invasion have distinct requirements for Rho/ROCK signalling and extracellular proteolysis. *Nat. Cell Biol.* 5:711–719. https://doi.org/10.1038/ncb1019

Salbreux, G., G. Charras, and E. Paluch. 2012. Actin cortex mechanics and cellular morphogenesis. *Trends Cell Biol.* 22:536–545. https://doi.org/10.1016/j.tcb.2012.07.001

Sedzinski, J., M. Biro, A. Oswald, J.Y. Tinevez, G. Salbreux, and E. Paluch. 2011. Polar actomyosin contractility destabilizes the position of the cytokinetic furrow. *Nature.* 476:462–466. https://doi.org/10.1038/nature10286

Sroka, J., I. Krecioch, E. Zimolag, S. Lasota, M. Rak, S. Kedracka-Krok, P. Borowicz, M. Gajek, and Z. Madeja. 2016. Lamellipodia and membrane blebs drive efficient electrotactic migration of rat Walker carcinosarcoma cells WC 256. *PLoS One.* 11:e0149133. https://doi.org/10.1371/journal.pone.0149133

Suraneni, P., B. Rubinstein, J.R. Unruh, M. Durnin, D. Hanein, and R. Li. 2012. The Arp2/3 complex is required for lamellipodia extension and direc-tional fibroblast cell migration. *J. Cell Biol.* 197:239–251. https://doi.org/10.1083/jcb.201112113

Svitkina, T. 2016. Imaging cytoskeleton components by electron microscopy. *Methods Mol. Biol.* 1365:99–118. https://doi.org/10.1007/978-1-4939-3124-8_5

Svitkina, T.M. 2017. Platinum replica electron microscopy: Imaging the cytoskeleton globally and locally. *Int. J. Biochem. Cell Biol.* 86:37–41. https://doi.org/10.1016/j.biocel.2017.03.009

Svitkina, T. 2018. The actin cytoskeleton and actin-based motility. *Cold Spring Harb. Perspect. Biol.* 10:a018267. https://doi.org/10.1101/cshperspect.a018267

Svitkina, T.M., A.A. Shevelev, A.D. Bershadsky, and V.I. Gelfand. 1984. Cytoskeleton of mouse embryo fibroblasts. Electron microscopy of platinum replicas. *Eur. J. Cell Biol.* 34:64–74.

Tournaviti, S., S. Hannemann, S. Terjung, T.M. Kitzing, C. Stegmayer, J. Ritzerfeld, P. Walther, R. Grosse, W. Nickel, and O.T. Fackler. 2007. SH4-domain-induced plasma membrane dynamization promotes bleb-associated cell motility. *J. Cell Sci.* 120:3820–3829. https://doi.org/10.1242/jcs.011130

Tyson, R.A., E. Zatulovskiy, R.R. Kay, and T. Bretschneider. 2014. How blebs and pseudopods cooperate during chemotaxis. *Proc. Natl. Acad. Sci. USA.* 111:11703–11708. https://doi.org/10.1073/pnas.1322291111

Wolf, K., I. Mazo, H. Leung, K. Engelke, U.H. von Andrian, E.I. Deryugina, A.Y. Strongin, E.B. Bröcker, and P. Friedl. 2003. Compensation mechanism in tumor cell migration: mesenchymal-amoeboid transition after blocking of pericellular proteolysis. *J. Cell Biol.* 160:267–277. https://doi.org/10.1083/jcb.200209006

Wu, C., S.B. Asokan, M.E. Berginski, E.M. Haynes, N.E. Sharpless, J.D. Griffith, S.M. Gomez, and J.E. Bear. 2012. Arp2/3 is critical for lamellipodia and response to extracellular matrix cues but is dispensable for chemotaxis. *Cell.* 148:973–987. https://doi.org/10.1016/j.cell.2011.12.034

Yang, C., and T. Svitkina. 2011. Filopodia initiation: focus on the Arp2/3 complex and formins. *Cell Adhes. Migr.* 5:402–408. https://doi.org/10.4161/cam.5.5.16971

Yoshida, K., and T. Soldati. 2006. Dissection of amoeboid movement into two mechanically distinct modes. *J. Cell Sci.* 119:3833–3844. https://doi.org/10.1242/jcs.03152